Rare Metal Materials and Engineering

Science Press

ARTICLE

DOI: 10.12442/j.issn.1002-185X.20240452.

Microstructure and mechanical properties of transient liquid-phase diffusion bonded GH5188 joint using a BNi-5 interlayer

Zilong Guo[1,2#], Zhaoxi Li[1,2#], Wei Guo[1*], Pengkun Liu[1,2], Jinglong Li[1*], Jiangtao Xiong[2]

[1] *State Key Laboratory of Solidification Processing, Northwestern Polytechnical University, Xi'an 710072, China*

[2] *Shaanxi Key Laboratory of Friction Welding Technologies, Northwestern Polytechnical University, Xi'an 710072, China*

[#] *These authors contributed equally: Zilong Guoa,b, Zhaoxi Lia,b*

[*] *Corresponding author: Jinglong Li (lijinglg@nwpu.edu.cn); Wei Guo (nwpuweiguo@nwpu.edu.cn)*

Abstract: This study focuses on the transient liquid phase (TLP) diffusion bonding of GH5188, utilizing a BNi-5 interlayer. Parameters were chosen and optimized for GH5188 alloy and the TLP joining mechanism. The microstructure evolution and mechanical properties of the joints were comprehensively examined. The relatively complete isothermal solidification zone (ISZ) ensured a reliable connection of the base metal (BM). In 1110 °C to 1190 °C, higher bonding temperature widened the ISZ and enhanced joint composition homogenization, improving mechanical properties. However, an increase in precipitated adversely affected the joint's mechanical properties. The maximum shear strength, reaching 482 MPa, was achieved at 1130 °C, representing 84.6% of the BM strength. Within the pressure range of 5 MPa to 15 MPa, both precipitation phases in the ASZ and voids generated by partial melting increased. On the contrary, their sizes decreased significantly with higher bonding pressure, resulting in an upward trend in alloy mechanical properties. The maximum shear strength of 490 MPa was attained at a bonding pressure of 15 MPa. The joint exhibited a typical mixed fracture pattern, with the small brittle $M_{23}C_6$ phase and voids significantly impacting mechanical properties. Nanoindentation tests indicated the ASZ as a potential source of cracks.

Key words: Transient liquid phase diffusion bonding, GH5188 cobalt-based superalloy, BNi-5 interlayer, Microstructure evolution, Mechanical property

Cobalt-based superalloys demonstrate exceptional properties, including superior creep resistance, corrosion resistance, thermal fatigue resistance, and high-temperature strength [1-2]. These alloys use Co as the matrix element and incorporate significant amounts of Ni, Cr, W, along with smaller quantities of Mo, La, Ti, and others. Compared to nickel-based superalloys, cobalt-based superalloys offer higher thermal conductivity and a lower thermal expansion coefficient, making them essential for applications requiring thermal fatigue resistance [4-6]. GH5188, a specific cobalt-based superalloy, demonstrates exceptional corrosion resistance, thermal fatigue resistance, and mechanical properties at elevated temperatures. Primarily employed in the fabrication of gas turbine components, such as combustion chamber walls, outer walls, seals, and exhaust nozzles [7-9], GH5188 plays a crucial role in advanced manufacturing fields. Therefore, the development of a reliable and effective bonding method for this material significantly influences its application in these vital and cutting-edge areas.

Transient liquid phase bonding (TLP) combines the advantages of diffusion bonding and brazing, consequently becoming a promising method for bonding GH5188. This approach enhances the alloy's applicability in crucial advanced fields [14-16]. Wei's investigation [34] into the microstructure and mechanical properties of GH5188 through selective laser melting revealed that the superior elongation of the joint was attributed to the presence of fine, non-brittle carbides, preventing premature fracture and enhancing ductility before necking. Additionally, Pouranvari's [31] study on the TLP

Received date:
Foundation item:
Corresponding author:

bonding of the Ni-based IN718 superalloy highlighted the significant influence of solidification (including isothermal and non-thermal processes) on bonding time. The distribution of the eutectic structure played a crucial role in determining the mechanical properties of the joint. Under eutectic-free conditions, where isothermal solidification was completed, the shear strength of the joints was controlled by the hardness of the ISZ, itself influenced by bonding temperature. Through proper design of process parameters, TLP diffusion bonding can obtain joints with comparable tensile and shear strength to the base metal [18-24]. Despite extensive research on TLP diffusion bonding of nickel-based superalloys, the reports on the TLP diffusion bonding of GH5188 alloy still remain lacking. It is unclear how TLP process parameters affect the interfacial properties, microstructure evolution, and mechanical properties of the GH5188 joint. Therefore, conducting an in-depth study of TLP diffusion bonding technology for GH5188 holds great significance in advancing its engineering applications.

This paper investigates the TLP of GH5188 superalloy using a BNi-5 interlayer. Multiple parameters were used taking the features of GH5188 alloy's component and the TLP joining mechanism into consideration. The microstructure of the typical interface and mechanical properties of the joint were comprehensively evaluated. The parameters optimization and the evolution of the microstructure, formation mechanism, mechanical properties and strengthening mechanism of the TLP diffusion bonded joint were discussed comprehensively.

1 Experiment

The base material (BM) was hot-rolled GH5188 sheet, with a tensile strength and a shear strength of 950 MPa and 570 MPa. The specific composition was shown in Table 1. The BNi-5 filler alloy was chosen as the interlayer, melting point is 1080 ℃-1135 ℃ with a specific composition shown in Table 2. The brazing material was mixed with an organic binder and coated on the surface to be bonded with a thickness of 50 μm. Before the bonding, GH5188 was cut to the desired size of 50 mm × 25 mm using a wire cutter, and was then polished step by step with sandpaper of 80#, 160#, 240#, 600#, 1000#, 1200#, 1500#, and 2000# to obtain a mirror finish by polishing with a 2.5 μm grinding paste. Then, put into an acid solution for acid pickling, then wiped with alcohol and blown dry with cold air. The joint was assembled as shown in Fig.1, and graphite compression heads were used for the upper and lower compression heads. Mica sheets were used as the barrier layers between the specimens, the compression heads and the gaskets. The diffusion bonding equipment used for the test was the radiation heating bonding machine. The metallographic morphology of the joints' interfaces was observed by scanning electron microscopy (ZEISS Sigma 300), and the elements in the bonding zone and precipitated phases were analyzed by the energy spectrum analyzer and the electron probe (JXA-8530F Plus). The shearing tests were conducted using the Instron-3382 universal testing machine. The morphologies of the joint fracture interface and the longitudinal section were analyzed by Helios G4 CX scanning electron microscope to analyze the fracture behavior of the joints.

To accelerate the interdiffusion between the interlayer and the BM, the bonding temperature should be elevated. However, to prevent the abnormal grain growth caused by the elimination of pinning effect, the bonding temperature must be kept below the solid solution temperature of $M_{23}C_6$. Therefore, the optimal bonding temperature range is 1110° C to 1190° C, with a 20 °C interval. Considering the yield condition and small deformation requirements at high temperatures, a reasonable range of pressure and bonding time should be selected, and finally the former was selected to be 5 MPa, 10 MPa and 15 MPa, and the latter was set to be 30 and 60 min. For the post-bonding heat treatment, the temperature was chosen to be 1000 °C and the required time is referred as the bonding time. this stage was designed for the diffusion between the BM and interlayer.

Table 1 Chemical Composition of GH5188(wt.%).

Element	Co	C	Si	Ni	Cr
Content	Bal	0.05-0.15	0.20-0.50	20-24	20-24
Element	W	La	Fe	Ni	
Content	13-16	0.03-0.12	⩽3	⩽1.25	

Table 2 Composition and Melting Temperature Range of BNi-5 Brazing Material(wt.%).

Element	Ni	Cr	Si	Co
Content	Bal.	18.5-19.5	9.75-10.5	0.10

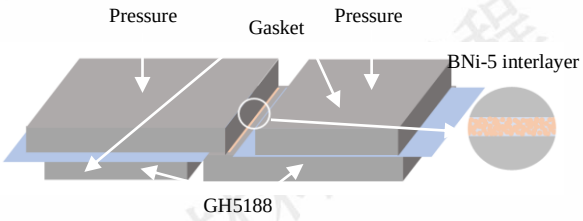

Fig. 1. Bonding assembly schematic diagram.

2 Results and Discussion

2.1 Typical joint microstructure

Fig. 2 illuminates the microstructure of the bond achieved at 1130 °C, 10 MPa bonding pressure, and 1h homogenization. The bonding interface is distinctly divided into four regions: Zone 1, 2, 3 and 4, representing the non-isothermal solidification zone (ASZ), ISZ, diffusion-affected zone (DAZ), and base metal (BM), respectively. Notably, there is an absence of large-scale continuous eutectic structure resulting from non-isothermal solidification (Fig. 2(a)). Additionally, the

BNi-5 solder alloy, containing a relatively high Si content, readily forms silicide with Cr, Co, and W.

The distribution of precipitated phases in the four regions shows significant variations. The ASZ has a small amount of large gray phase A and white phase B surrounded by phase A. The ISZ exhibits a uniform microstructure with a small amount of gray phase C. The DAZ contains numerous white strip phase D, while the BM area has a small amount of white precipitate (E). To ascertain the composition of the precipitated phases, an energy dispersive X-ray electroscope (EDS) analysis was conducted on the bond zone (Fig. 3). The analysis reveals that the Ni content in the joint weld zone is higher than that in the BM area, while the contents of Co, W, and Si are lower (Fig. 3). Specifically, the matrix in the BM area is identified as γ-Co, whereas the ISZ matrix is γ-Ni. The precipitated phase in the DAZ exhibits higher Si and W content than the BM, with lower contents of Ni, Co, and Mn. Notably, precipitate A near the ISZ has a high Cr content. EDS point scanning performed in each region indicates that, except for the white precipitate (E) in the BM area, the Si content in other precipitates exceeds 11% (Table 3).

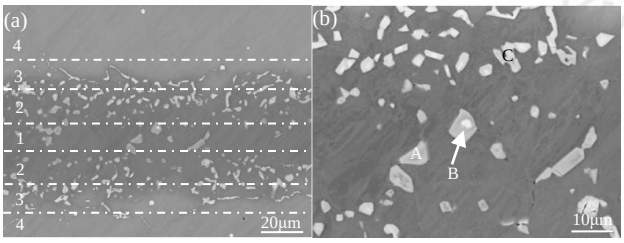

Fig.2. The microstructure of the joint under 1130°C -10MPa-60min with BNi-5 interlayer: (a) microstructure morphology diagram, (b) magnified microstructure of the red area in (a).

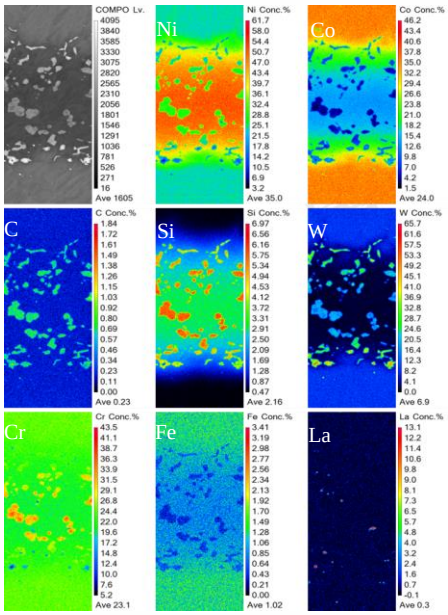

Fig. 3. EPMA elemental analysis of the joint under 1130°C -10MPa-60min.

The primary composition element in the joint bond zone is Ni, and considering that the solubility of Si in Ni is only 8%, it indicates that the precipitated phases in the ASZ, ISZ and DAZ are Si-rich. Furthermore, EPMA results reveal higher C content in the precipitated phases in the ASZ, ISZ and DAZ. Since C and Si are chemically similar, they preferentially precipitate at the same location. The Cr content in precipitate A was found to be 35.03%, and EPMA results indicated an enrichment of W. Hence, precipitate A is identified as an $M_{23}C_6$ compound rich in Cr and W. Surrounding precipitate A, precipitate B exhibited a W content of 26.79%, suggesting that it is a type of M_6C compound. Rao [25] explained that the Cr content of M_6C-type compounds does not reach the average content in the alloy, leading to the emission of a substantial amount of Cr outward during the formation of M_6C-type compounds. Consequently, the $M_{23}C_6$ silicides grows along the M_6C lattice direction, ultimately forming a pseudo-eutectic precipitate composed of $M_{23}C_6$ and M_6C silicides. The W content in precipitates D and E was determined to be 18.59% and 31.18%, respectively. Building upon previous elemental analyses, it can be inferred that white precipitates D and E are both M_6C silicides.

The $M_{23}C_6$ mainly precipitates in the ISZ, while M_6C precipitates in the DAZ in addition to eutectic precipitation with $M_{23}C_6$ in the ISZ. The statistical analysis of the volumes of the two revealed that the size distribution of $M_{23}C_6$ is between 3-10 μm, while the size of M_6C is mostly 1-3 μm. The interface embedded with the precipitates of $M_{23}C_6$ silicides and M_6C silicides statistically accounts for approximately 26% of the whole interface, obtained by observing the straight interface. In addition, this statistical method is frequently used to calculate the bonded ratio evaluating the quality of diffusion-bonded joints.

Table 3 Composition of the precipitated phases at various positions in Fig. 2 (at.%)

Position	C	Si	Cr	Mn	Co	Ni	W
A	0.6	13.9	35.0	2.4	7.1	32.4	8.6
B	0.9	12.1	24.1	1.4	9.1	25.7	26.8
C	0.4	11.0	23.1	2.4	15.9	44.2	1.6
D	0.7	11.5	17.8	1.5	18.5	31.0	18.6
E	0.8	-	22.8	0.8	33.0	11.6	31.2

Richer information about the ISZ is illustrated by TEM analysis. High-resolution (HR) HADDF-STEM images show unique advantages in detecting fine phases composed of different chemical elements. Fig. 4(b) shows the matrix phase is rich in Co and Ni, which is confirmed by the EPMA characterization results and the SAED pattern from the [1, 1, 0] zone axis (Fig. 4(e)) to be an FCC structure (a = 0.3596 nm). That is, Ni-rich solid solution, γ phase. In addition, Cr, W and C are relatively enriched in white phase B, and the composition of

the precipitate is shown in Table 3. In Fig.4, it was determined that the precipitate was an $M_{23}C_6$ silicide with a face-centered cubic structure (FCC) (M represents the transition elements Cr, Mo, W and Re). The interplanar spacing of $(1, \bar{1}, 0)$ FCC is 0.523 nm. HRTEM shows lattice fringes with different spacing (Fig. 4(c)). Filtered inverse fast Fourier transform (IFFT) pattern shows clear details. HRTEM, fast Fourier transform (FFT) spectra and inverse Fourier transform (IFFT) images show that at the interface between the precipitated $M_{23}C_6$ silicide (FCC) and the γ matrix (FCC). The joint strength is effectively matched with the TEM-EDS analysis results.

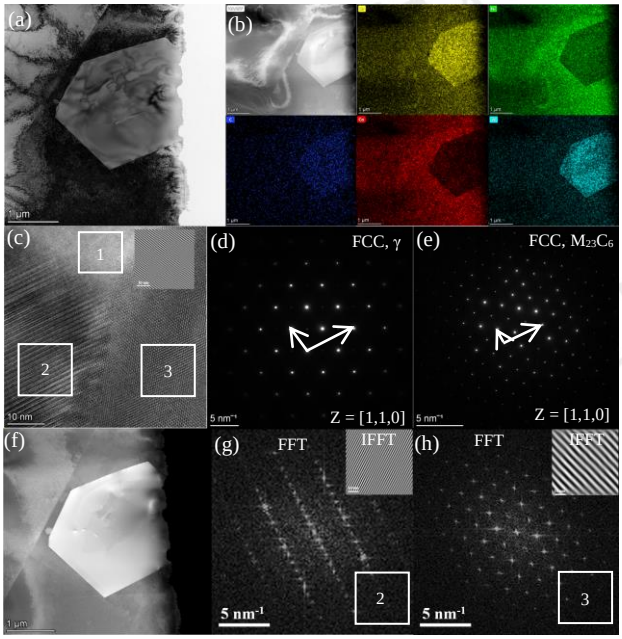

Fig. 4. TEM characterization of a local area of the ISZ in Fig.2 (a): (a) BF image, (b) HAADF pattern and element distribution, (c) localized HRTEM pattern with (d) and (e) SEAD pattern in BM and precipitate respectively, (f) HADDF diagram corresponding to (c) and the FFT and IFFT diagrams (g) and (h) corresponding to the rectangular box in (c).

2.2 Influence of the parameters on the joint microstructure

The bonding pressure was maintained at 10 MPa, with an bonding time of 1 h. The study involved five temperatures, specifically 1110 °C, 1130 °C, 1150 °C, 1170 °C, and 1190 °C. The joint morphology at 1130 °C was previously examined in the preceding section and will not be reiterated here.

As the bonding temperature rises, there is an observable increase in the precipitates within the ISZ. During the isothermal solidification, a ISZ layer forms between the intermediate phase and the BM due to the influence of isothermal solidification (Fig. 5). The Melting Point Depressant (MPD) element in the intermediate liquid phase must diffuse into the BM through the ISZ to continue facilitating the progress of isothermal solidification [21]. In the initial stages, a higher bonding temperature promotes the diffusion of the MPD element in the intermediate liquid phase, leading to increased dissolution in the adjacent BM area. This results in a thicker intermediate liquid phase zone, which gradually transforms into the ISZ during isothermal solidification. Consequently, the MPD elements in the intermediate liquid layer need to diffuse further into the substrate to be consumed, but their diffusion slows down in the solid phase. This reduction in diffusion rate in the solid phase contributes to a decrease in the isothermal solidification rate of the joint. Consequently, a longer bonding time is necessary to eliminate joint eutectic structures that have not completed isothermal solidification. In summary, as the bonding temperature increases, the dissolution of the BM intensifies, leading to an increased width of the formed ISZ. This, in turn, results in a decreased isothermal solidification rate, while the aggregation and precipitate formation of MPD elements increase.

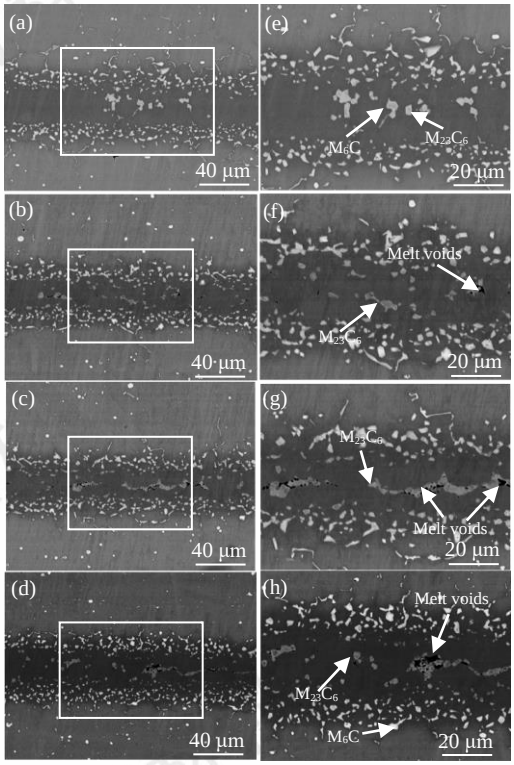

Fig. 5. Microscopic morphology of the joint under temperatures of 1110 °C, 1150 °C, 1170 °C, and 1190 °C respectively ((a) to (d)) and their corresponding high magnification micrographs of the red region ((e) to (h)).

As the bonding temperature rises, especially beyond 1130 °C, micro-voids tend to appear in the ASZ near the precipitate. The eutectic phase in the alloy, having a lower melting point than the alloy itself, undergoes pre-melting during high-temperature solid solution treatment. This pre-melting occurs below the theoretical melting point of the alloy [28]. Resultantly, voids form near the pre-melted eutectic phase, serving as potential sources for crack initiation and negatively

impacting alloy performance. To address this, an appropriate heat treatment method, such as low-temperature pre-treatment, should be chosen to fully dissolve the eutectic phase. However, if the selected heat treatment temperature doesn't reach the alloy's eutectic temperature, partial melting may occur due to incomplete dissolution into the BM matrix. With increasing bonding temperature, the likelihood of partial melting rises, leading to an increased number of precipitates and voids.

For the precipitate phases in the joint structure, this article performed EDS spectrum analysis on the joint area at 1150 °C. No variation in the types of precipitates was observed compared to at 1130 °C (Fig. 6). In the ISZ, the precipitate phase is identified as an $M_{23}C_6$ silicide rich in Cr and W, while in the DAZ, the precipitate phase is an M_6C silicide enriched in W. The increase in temperature did not significantly change the distribution and size of the precipitated phases. The sizes of $M_{23}C6$ and M_6C were still 3-10μm and 1-3μm.

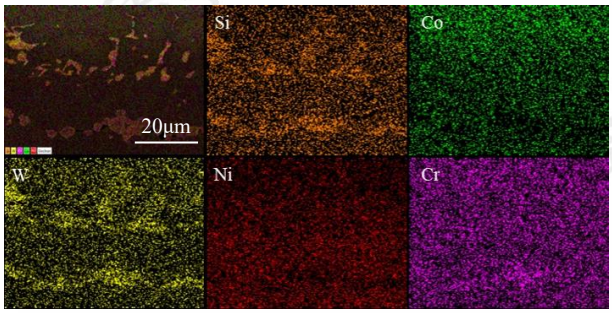

Fig. 6. Elemental distribution of joint structure at bonding temperature of 1150 °C.

At 1150 °C with a bonding time of 1 h, the microstructure of the joint is depicted in Fig. 7. Isothermal solidification is accomplished under different bonding pressures (5 MPa, 10 MPa, 15 MPa). Simultaneously, an increase in bonding pressure correlates with a reduction in the size of the precipitation phase and voids within the ASZ, while their quantity rises, as the bonding pressure increases from 5 MPa to 15 MPa, the size of $M_{23}C_6$ decreases from 3-14 μm to 2-6 μm. The diminished size of the precipitation phase may be attributed to heightened bonding pressure facilitating element diffusion, thereby decreasing the aggregation of elements and resulting in smaller precipitation phases. Conversely, the heightened precipitation phase contributes to an increased number of voids dissolved by it. However, the size of the precipitation phase constrains the size of the voids, resulting in a decrease in void size as the precipitation phase size decreases.

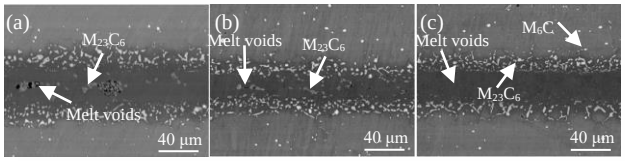

Fig. 7. Microstructure of the joints under different bonding pressures (a) 5 MPa, (b) 10 MPa, (c) 15 MPa.

In Fig. 8(a-c), the orientation and deformation distribution of the joint are depicted. With an increase in bonding pressure, the interface between BNi-5 and GH5188 gradually diminishes. At 15 MPa bonding pressure, it becomes challenging to discern the bonding interface, indicating substantial mutual diffusion between BNi-5 and GH5188. The diffusion rate of elements is directly proportional to the pressure applied, and the mutual diffusion coefficient between elements increases with higher pressure. The degree of recrystallization in the joint intensifies with increased bonding pressure (Fig. 8(d-f)). Moderate pressurization facilitates grain boundary movement and grain rearrangement, promoting the recrystallization process. As bonding pressure rises, the dislocation density at the joint gradually increases, leading to an accumulation of stress. Some grains undergo recrystallization, resulting in a reduction of dislocation density and the release of accumulated stress [35]. Moreover, at 15 MPa bonding pressure, the specimen's deformation has reached the predetermined maximum, and further increasing the bonding pressure might cause excessive deformation, prompting the experiment to refrain from employing a higher bonding pressure.

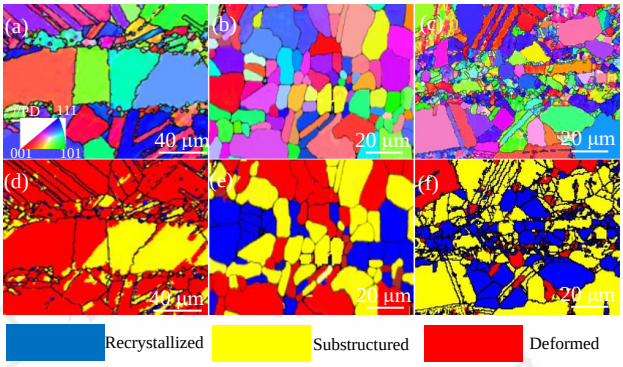

Fig. 8. EBSD images of the joints at different bonding pressures: IPF: (a) 5 MPa, (b) 10 MPa, (c) 15 MPa; RF:(d) 5 MPa, (e) 10 MPa, (f) 15 MPa.

The microstructure of the joint under different parameters is illustrated in Fig. 9. Joints held for 30 min and 60 min have both achieved a high degree of isothermal solidification, resembling the joint microstructures obtained under various bonding temperatures in the preceding sections. Precipitation phases are present in the ISZ and ASZ, and some of these phases in ASZ are accompanied by voids, as explained earlier. This indicates that precipitation phases and voids persist even after 30 min and 60 min of bonding time. The observed persistence suggests that the selected temperature in this study might result in partial melting of the precipitation phase.

For joints with a bonding temperature of 1190 °C, a bonding pressure of 5 MPa, and no homogeneity time, the microstructure exhibits a large incomplete isothermal solidified eutectic structure in ASZ (Fig. 10). This lager degree of incomplete solidification occurs because isothermal solidification

did not fully complete, and the remaining portion of the intermediate liquid phase underwent cooling and solidification processes. As a result, a brittle eutectic with a low melting point formed, adversely affecting the mechanical properties of the joint [23]. To confirm the composition of the ASZ, EDS spectral analysis was conducted (Fig. 10). The low melting point eutectic structure in the ASZ exhibits higher contents of Ni and Si, while the contents of Cr and Co are relatively low, indicating uneven element diffusion. Ni and Si from the BNi-5 brazing material are still abundantly present in the eutectic structure. The distribution of precipitation phase element content in the ISZ and diffusion influence zone resembles that of the previously observed precipitation phase. The precipitation phase in the ISZ exhibits enrichment of W and Cr, forming an $M_{23}C_6$ type silicide. Meanwhile, the precipitation phase in the diffusion influence zone is enriched with W, forming an M_6C type silicide.

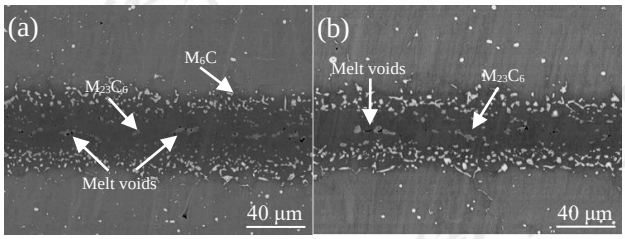

Fig. 9. Microstructure of the joint under different bonding times (a) 30 min, (b) 60 min.

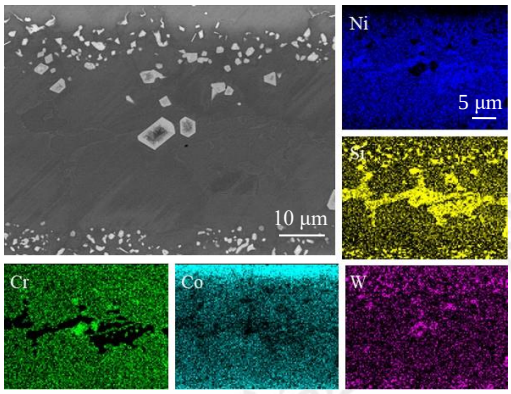

Fig. 10. EDS elemental analysis of the joint at 1190 °C /5 MPa.

2.3 Effect of bonding parameters on mechanical properties

Fig. 11 illustrates the tensile and shear strength of the joint at different temperatures, maintaining a fixed homogenization time of 1 h and a bonding pressure of 10 MPa. The tensile and shear strength exhibit a trend of increase followed by a decrease. At a bonding temperature of 1130 ℃, both tensile and shear strength reach their maximum value at 482 MPa, equivalent to 84.6% of the tensile strength of the BM. This peak strength can be attributed to the reduction in the size of silicides and voids in the ASZ. Silicides exhibit hardness and brittleness, rendering them resistant to plastic deformation under compressive shear loads. This resistance results in stress concentration, which initiates cracks. The stress concentration at the void tips further enhances crack nucleation, leading to crack propagation and coalescence with neighboring cracks, ultimately resulting in joint failure. Reducing the size of silicides generates a pinning effect on dislocations. Additionally, the reduction in void size alters their shape from elliptical to circular, decreasing the stress concentration at the void tips and consequently enhancing joint strength. In addition, the mechanical properties of the joint are closely related to its grain size. As the temperature increases, the grain size at the joint gradually enlarges. At 1190 °C, compared to the bonding temperature of 1110 °C, a substantial growth in grain size is observed, leading to a deterioration in the mechanical properties of the joint (Fig. 13). The BNi-5 brazing metal has a melting temperature range of 1080 °C-1135 °C. At bonding temperatures between 1110-1130 °C, small gaps and cracks form at the joint due to the initial melting of BNi-5 solder with poor wettability and fluidity, resulting in underfilling in the edge area. The diffusion of elements in the joint area is insufficient at lower temperatures, unlike at 1130 °C, where the bonding temperature is more suitable for element diffusion (Fig. 3, 6). Consequently, achieving homogenization of the joint composition and obtaining fine microstructures is challenging at lower bonding temperatures, resulting in poorer mechanical properties.

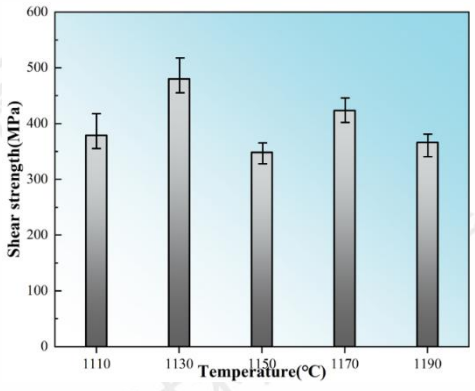

Fig. 11. Shear strength of joints at different bonding temperatures.

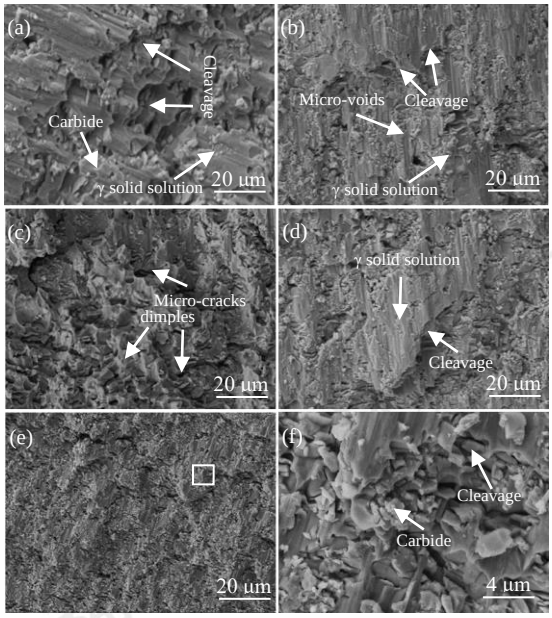

Fig. 12. Characteristics of joint fracture morphology at different bonding temperatures: (a) 1110 °C, (b) 1130 °C, (c) 1150 °C, (d) 1170 °C, (e) 1190 °C, and (f) high magnification microscopic image of the red area in Fig. (e).

The microstructures of the joint fracture surfaces in Fig. 12 (a), (b), (d), and (e) exhibit similarities, featuring a rough surface with facet features typical of cleavage fractures. Fig. 12 illustrates that the cleavage crack at the fracture origin occurs in the silicide phase. The plastic deformation capacity of the silicide precipitation at grain boundaries is different from that of the matrix phase. This disparity results in uncoordinated deformation during the shearing process, causing stress concentration. The stress concentration damages the plastic toughness of the grain boundaries, induces cracks at the grain boundaries, and propagates along these boundaries. Ultimately, this process leads to brittle fracture and failure of the joint. Additionally, a significant presence of precipitated phases is observed on the fracture surface. Precipitates share similar chemical compositions, being rich in C and W, and exhibit M_6C silicides (Fig. 12(f)). Joints bonded at 1150 °C display a pitted structure in the fracture area, showcasing a ductile-brittle mixed fracture unlike other bonding temperatures (Fig. 12(c)). However, some cracks are apparent on the fracture surfaces, which may account for the lower tensile and shear strength of the joint bonded at 1150 °C.

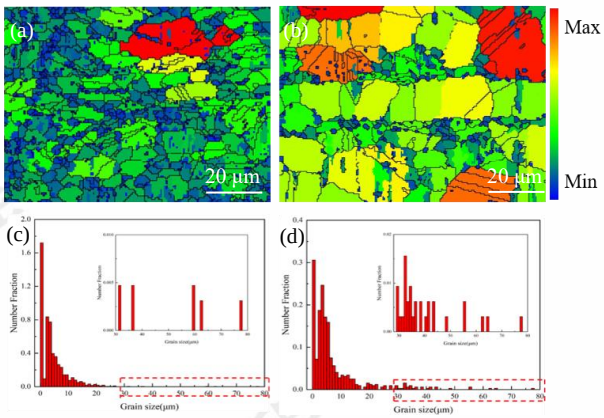

Fig. 13. The contours of joints under different temperatures: (a) 1100 °C/60 min, (c) 1190 °C/60 min; and the grain size bar charts: (b) 1100 °C/60 min, (d) 1190 °C/60 min.

Fig. 14 illustrates the shear strength of the joint under various bonding pressures, homogenize for one hour and maintaining a temperature of 1150 °C. The joint's shear strength is minimal at 5 MPa and reaches its maximum at 15 MPa, achieving 490 MPa. This value represents 86% of the shear strength of the BM.

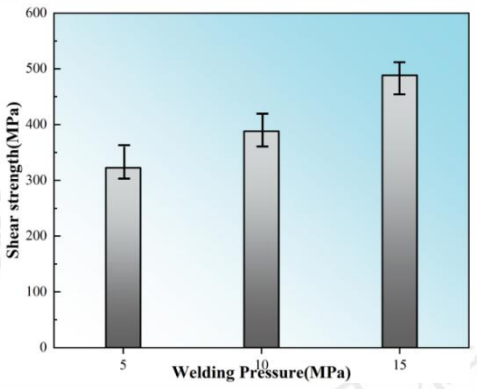

Fig. 14. Shear strength of the joints under different pressures.

The joint shows a higher number of silicides in the ISZ compared to the joint bonded at 5 MPa. However, the corresponding silicide size in joints bonded at 10 MPa is considerably smaller, rendering it less susceptible to fracture. Furthermore, the smaller silicide size serves as a pinning site for dislocations, contributing to enhanced mechanical properties of the alloy. Consequently, the joint displays slightly greater tensile and shear strength compared to the joint bonded at 5 MPa.

Fig. 15 depicts the fracture surfaces of the joint. Upon closer examination at high magnification (Fig. 15(b)), the presence of pits is evident. Similar pits were observed on the fracture surfaces of joints bonded at 10 MPa and 15 MPa bonding pressures. However, areas with rough surfaces, pronounced undulations, and stepped features typical of cleavage fracture

are also noticeable. The proportion of areas exhibiting cleavage fracture decreases with increasing bonding pressure, while the tendency towards ductile fracture gradually increases. This trend contributes to enhancing the properties (Fig. 15(a, b, d)).

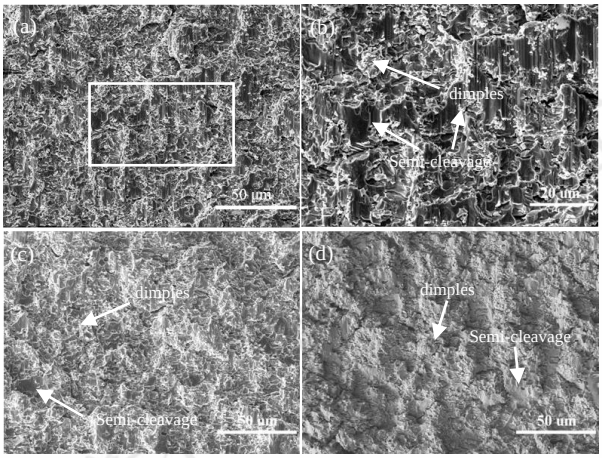

Fig. 15. Characteristics of joint fracture morphology under different bonding pressures: (a) 5 MPa, (b) High magnification microscopic image of the red area in Fig. (a), (c) 10 MPa, (d) 15 MPa.

Tensile-shear tests were performed on joints bonded at 1150 °C and 5 MPa bonding pressure under different bonding times. The results revealed that the joint held for 0.5 h had 355 MPa, while the joint held for 1 h had 321 MPa, indicating minimal difference between the them. This observation aligns with the relatively small differences in microstructure between the joints held for 0.5 h and 1 h, as evident in the previous section. Based on these findings, it can be concluded that bonding time has a relatively modest effect on the microstructure and mechanical properties when the bonding time ranges from 0.5 h to 1 h. In the absence of homogenization time, the joint is susceptible to cracking during the shearing process due to the incomplete ASZ at the joint.

2.4 Mechanism of the joint formation

The TLP diffusion bonding process of GH5188 alloy can be delineated into four stages, encompassing the melting of the intermediate layer, dissolution of the BM, isothermal solidification, and composition homogenization. A comprehensive analysis of the microstructure and phase changes of the joint at each of these four stages will be presented in detail (Fig. 16).

(1) Melting of the intermediate layer: In the TLP diffusion bonding process, the selected bonding temperature surpasses the minimum melting point range of the BNi-5 solder (1080 °C -1135 °C), causing the intermediate layer solder to transform into a liquid phase before reaching the set temperature. However, solid-state diffusion takes place in the intermediate layer as it contacts the BM during the heating process. Si preferentially diffuses into the BM, creating concentration differences in Si distribution within the intermediate layer. This results in higher concentrations in the middle area and lower concentrations on both sides. Consequently, the actual melting temperature is lower in the middle and higher on both sides. Therefore, the central part of the intermediate layer will undergo melting first upon reaching the liquidus temperature. Subsequently, the liquid phase will propagate to both sides as the temperature continues to rise until complete melting is achieved.

(2) Dissolution of the BM: Following the complete melting of the intermediate layer, a liquid layer forms between the two BM. If the bonding temperature set at this stage is too low, insufficient wetting and spreading of the BNi-5 solder may occur, leading to the presence of numerous unfilled voids. As the liquid intermediate layer spreads entirely, robust element diffusion transpires between the liquid phase and the two BM. Concurrently, the diffusion of Co and W leads to a decrease in the melting point of BM near the interface. When the actual melting point falls below the bonding temperature, the BM in this region dissolves, expanding the liquid phase area and facilitating diffusion into the BM. The continuous diffusion between the liquid intermediate layer and the BM causes the liquid phase area to expand, and the concentration of the MPD element proportionally decreases [26].

(3) Isothermal solidification: Following the complete melting of the intermediate layer, three phenomena occur in the joint: Si diffusion to the substrate, the diffusion of elements in the base metal into the liquid phase, and the entry of elements into the liquid phase due to substrate dissolution. These phenomena determine the liquidus temperature of the liquid phase. The impact of these processes depends on the distribution coefficient. Given that the distribution coefficient of Si is less than 1, the temperature of the liquidus increases as the concentration of Si in the liquid phase decreases. Simultaneously, the enrichment of Cr, Mo, and Ti, with distribution coefficients larger than 1, BM dissolution and diffusion also contributes to an increased liquidus temperature [31]. The process of isothermal solidification will take place when the temperature of both is equal. Throughout isothermal solidification, mutual diffusion between the BM and the intermediate layer in the liquid phase stands as the primary driving force for composition changes.

(4) Composition homogenization: Typically, TLP diffusion bonded joints that have undergone isothermal solidification still exhibit notable differences in element concentration compared to the BM. Additionally, the joints may contain numerous silicides in the grain boundaries and grains of the DAZ. These silicides frequently serve as sources for crack initiation under load, consequently diminishing the joint's strength [33]. Hence, composition homogenization is often carried out during the bonding stage, and an excessively brief bonding time may impede the completion of this critical phase.

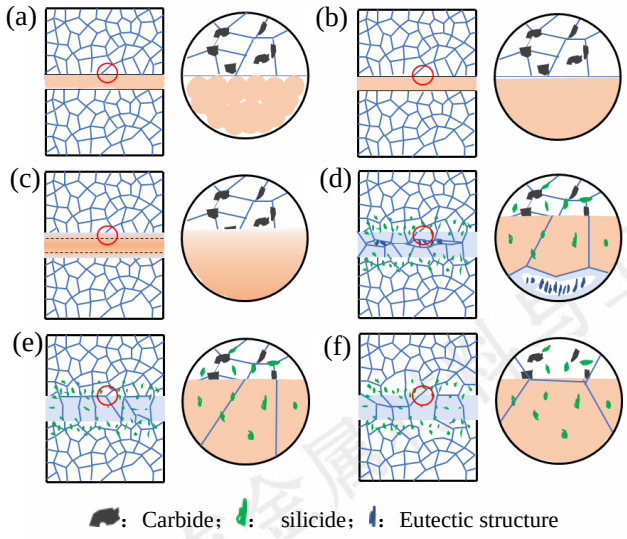

Fig. 16. Schematic diagram of formation process of GH5188 TLP bonded joint: (a) assembly Status, (b) melting of the intermediate layer, (c) melting of base material, (d) insufficient isothermal solidification, (e) isothermal solidification, (f) grain coarsening.

2.5 Joint strengthening mechanism

Based on the observed effects of bonding temperature, bonding pressure, and bonding time on joint shear strength, along with the analysis of fracture characteristics, the strengthening mechanism inherent in TLP diffusion bonding of GH5188 alloy with BNi-5 filler metal can be elucidated, as illustrated in Fig.17:

(1) Alloying of the joints: Beyond the fundamental element Ni, the BNi-5 soldered intermediate layer also incorporates alloying elements like Cr, Si, and Fe. The solid solubility of C in Ni is relatively significant, approximately 0.6 wt.%. Ni can solidify silicides and participate in joint formation, leading to solution strengthening. Simultaneously, the MPD element Si induces partial melting of the BM into the joint's liquid phase. This mitigates strength loss stemming from the diffusion of the strengthening element to the middle layer during solid-state diffusion bonding. Owing to the rapid diffusion rate of atoms in the liquid phase, a relatively uniform element distribution can be achieved. These elements contribute to the process of alloying isothermally solidified tissues. Nano-indentation tests were conducted to shed light on the distribution and evolution of the micro-mechanical properties across the bonding interface. The ASZ exhibits the highest hardness value, attributed to the presence of hard and brittle eutectic silicide. In comparison, the DAZ zone shows increased hardness due to the precipitation of Cr, Mo, and W borides. The ISZ zone, located at the center of the joint, has the lowest hardness value, primarily due to the low content of precipitate phases, which are mainly composed of γ solid solution. (Fig. 18(a)). The deformation of ASZ under load was significantly smaller than that of the adjacent ISZ region (Fig. 18(b)). As a result, stress concentrations are susceptible to in the ASZ area, which may lead to cracking of joints from the holes under tensile or shear stress.

(2) Inhibition of grain coarsening in the diffusion zone: In TLP diffusion bonding, while there is a reduction in the volume of certain grain boundary phases due to the diffusion of strengthening elements, the diffusion rate of Si from the intermediate layer to the BM is notably higher than others. Consequently, silicide can precipitate in both grains and grain boundaries, serving as effective pinning points to prevent grain coarsening in the diffusion zone. The examination of the joint's mechanical properties reveals the emergence of new cleavage planes due to the characteristics of cleavage fracture when passing through silicide. This alteration in the propagation path consumes more energy during the fracture process, contributing to the enhancement of joint strength [28]. In addition, the TEM results in Fig. 4 demonstrate that the precipitate phase in the ISZ is the $M_{23}C_6$ silicides of FCC structure (Fig. 4(e)), which can hinder grain boundary migration. Within the pressure setting range, with the increase of pressure, the number of precipitated phases in the ISZ increases and refines, and the pinning effect is continuously enhanced, and the size of the holes caused by the first melting also decreases due to the decrease of the size of the precipitated phase, which is conducive to the improvement of joint strength.

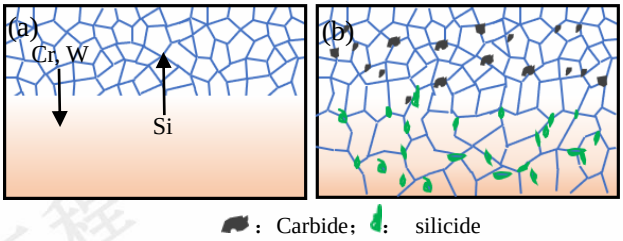

Fig. 17. Schematic diagram of joint strengthening mechanism:(a) Strengthening joint alloying, (b) Suppress grain coarsening in the diffusion zone.

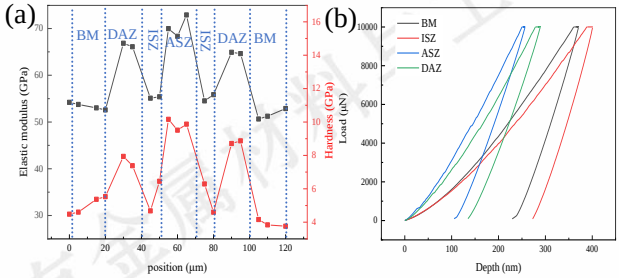

Fig. 18. Nanoindentation results for TLP bonded joints for 60 min at 1190 °C/5 MPa: (a) elastic modulus and hardness distribution over the entire bonding interface, (b) typical load-depth diagram.

Under the optimal bonding parameters of 1130 °C, 15 MPa, and 60 min, the BM and the interlayer elements achieved significant mutual diffusion, thereby markedly enhancing the alloying degree of the joint. The size of the precipitated phase was notably reduced under these conditions, which significantly increased the pinning effect on dislocations. Concur-

rently, the size of the voids was reduced, causing the void morphology to transition to a circular shape and decreasing the tip stress. As a result, these process parameters yielded the highest shear strength.

3 Conclusions

(1) Solid joints of GH5188 are achieved through TLP bonding utilizing BNi-5 solder. The bonding conditions include temperatures ranging from 1110 to 1190 °C, pressures between 5 to 15 MPa, and bonding times of 30 and 60 min. The microstructure characteristics of the joint consist of the ASZ, ISZ, DAZ, and BM. The results of TEM and EPMA tests showed that the precipitates in the base metal zone and the DAZ are M_6C silicides, while the primary precipitates in the ISZ are $M_{23}C_6$ silicides.

(2) Optimal microstructure development in the joint is favored by lower temperatures and higher pressures. With an increase in bonding temperature from 1130 °C to 1190 °C, there is a gradual increase in the precipitate phase within the ASZ and ISZ. Simultaneously, elevating the bonding pressure from 5 MPa to 15 MPa leads to an increase in the number of precipitated phases in the ASZ, accompanied by a decrease in their size. TLP is not sensitive to bonding time, and the change of bonding time in the selected range has no significant effect on the morphology and mechanical properties of the joint.

(3) The highest shear strength, reaching 490 MPa, is achieved at 1130 °C, 15 MPa, and 30 min. With an increase in bonding pressure from 5 MPa to 15 MPa, both tensile and shear strength exhibit an upward trend, primarily attributed to the reduction in the size of the precipitate phase and the voids of the ASZ. Fractography analysis revealed a typical mixed fracture mode, with various dimples and cleavage facets observed along the fracture. Consequently, the small brittle $M_{23}C_6$ phase and voids play a significant role in influencing the mechanical properties of the joints. Nanoindentation tests demonstrated mechanical variations across the bonding interface, with the ASZ identified as a potential source of cracks.

References

1 Lass EA, Sauza DJ, Seidman DN et al. Acta Materialia[J],2018 147:284–295.

2 Zhu LH, Xiao L, Guo JZ et al. Rare Metal Materials and Engineering [J], 2023 52: 2415-2423.

3 Ni HH, Zeng Q, Zhang K et al. Rare Metal Materials and Engineering[J], 2023 52: 2302-2308.

4 Zhang JG, Chen X, Li Z et al. Rare Metal Materials and Engineering [J], 2023 52: 1985-1993.

5 Zhang W, Chen ZS, Dong RF et al. Rare Metal Materials and Engineering[J], 2023 52: 3170-3178.

6 Kong WJ, Ding YT, Wang XM et al. Rare Metal Materials and Engineering[J], 2023 52: 2859-2868.

7 Lee WS, Kao HC. Materials Science and Engineering: A [J], 2014, 594: 292-301.

8 Zhen B, Kong WJ, Gao YB et al. Rare Metal Materials and Engineering[J], 2023 53: 563-571.

9 Ding YT, Wang T, Wang XM et al. Rare Metal Materials and Engineering[J], 2023 52: 2549-2558.

10 Tabaie S, Rézaï-Aria F, Flipo BCD et al. Materials Characterization[J], 2021, 171: 110766.

11 Liu YJ, Long TX, Guo CC. Rare Metal Materials and Engineering[J], 2023 52: 3522-3529.

12 Yang ZM, Chen ZJ, Lin YC et al. Rare Metal Materials and Engineering[J], 2023 52: 3147-3152.

13 Tabaie S, Rézaï-Aria F, Flipo BCD et al. Journal of Materials Science & Technology[J], 2022, 96: 248-261.

14 Li ZX, Li SW, Xiong JT et al. Journal of Manufacturing Processes[J], 2022, 84: 1331-1338.

15 Wang J, Zhang YW, Xiong YL et al. Rare Metal Materials and Engineering[J], 2022, 51(12): 4446-4451.

16 Tong L, Hong X, Yang WP et al. Rare Metal Materials and Engineering[J]. 2013 Jun 1;26(3):601-5.

17 Tsai C H, Hung H T, Chang F L et al. Journal of Materials Research and Technology[J], 2022, 19: 2510-2515.

18 Wang CY, Xing F, Liu XY et al. Rare Metal Materials and Engineering [J], 2023, 52(1): 323-331.

19 Song KJ, Ji YK, Wei Y et al. Rare Metal Materials and Engineering [J], 2023, 52(10): 3461-3469.

20 Zhao GY, Jin CB, Zhang RY et al. Rare Metal Materials and Engineering[J], 2021, 50(7): 2521-2527.

21 Liu J, Jin T, Zhao N et al. Materials Characterization[J], 2011, 62(5): 545-553.

22 Bakhtiari R, Ekrami A. Materials Characterization[J], 2012, 66: 38-45.

23 Wikstrom NP, Ojo OA, Chaturvedi MC et al. Materials Science and Engineering: A[J], 2006, 417(1-2): 299-306.

24 Nishimoto K, Saida K, Kim D et al. ISIJ International[J], 1995, 35(10): 1298-1306.

25 Rao KBS, Castelli MG. Metallurgical and Materials Transactions A[J], 1997, 28: 347-361.

26 Ghoneim A, Ojo OA. Materials Characterization[J], 2011. 62(1): 1-7.

27 Mostafaei, Abbasi. Journal of Alloys and Compounds[J], 2015, 648: 1031-1037.

28 Gao YW, Dong JX. Rare Metal Materials and Engineer-

ing[J],2017, 46 (10) : 2922-2928.

29 Yuan L, Xiong JT, Peng Y et al. Materials Characterization[J], 2021, 178: 111292.

30 Xia WS, Zhang Z Liang Y et al. Journal of Materials Science & Technology[J], 2020, 44: 76-95.

31 Pouranvari M, Ekrami A, Kokabi A H. Materials Science and Engineering: A[J], 2013, 568: 76-82.

32 Song WQ, Ren J, He P et al. Journal of Manufacturing Processes[J], 2021, 64: 1476-1483.

33 Zhang C, Li MQ, Li H et al. Journal of Manufacturing Processes[J], 2018, 35: 71-78.

34 Wei W, Xiao JC, Wang CF et al. Materials Science and Engineering: A[J], 2022, 831: 142276.

35 Liu D, Chai H, Yang L et al. Journal of Alloys and Compounds[J], 2022, 895: 162565.

36 Majumdar S,Sengupta P,Kale G B *et al.Surface and Coatings Technology*[J],2006,200:3713

添加BNi-5中间层的GH5188瞬态液相扩散焊连接接头的微观组织和力学性能研究

郭子龙[1,2]，李昭希[1,2]，郭伟[1]，刘朋坤[1,2]，李京龙[1]，熊江涛[2]

(1. 西北工业大学，凝固国家重点实验室，陕西西安 710072)

(2. 西北工业大学，摩擦焊陕西省重点实验室，陕西西安 710072)

摘　要：本研究重点关注 GH5188 的瞬态液相 (TLP) 扩散连接，采用 BNi-5 中间层。针对 GH5188 合金及 TLP 连接机理进行参数选择及优化。全面研究了接头的组织演变和力学性能。相对完整的等温凝固区（ISZ）保证了母材（BM）的可靠连接。在 1110℃至 1190℃范围内，较高的连接温度使 ISZ 增宽，促进了接头成分的均匀化，提高了力学性能。然而，析出相的增加对接头的力学性能产生了不利影响。在 1130℃时获得了最大的剪切强度，达到482MPa，占BM强度的84.6%。在5MPa至15MPa的压力范围内，ASZ 中的析出相和部分熔化产生的空隙均有所增加。相反，它们的尺寸随着连接压力的升高而显著减小，导致合金力学性能呈上升趋势。在 15MPa 的连接压力下获得了最大的剪切强度，为 490MPa。 MPa。接头表现出典型的混合断裂模式，小而脆的 M23C6 相和空隙显著影响机械性能。纳米压痕测试表明 ASZ 是裂纹的潜在来源。

关键词：瞬态液相扩散焊; GH5188钴基高温合金; BNi-5中间层; 组织演变; 力学性能

作者简介：郭子龙，男，2001 年生，硕士，西北工业大学，陕西 西安 710072，电话：19834533264，E-mail: guozilong@mail.nwpu.edu.cn